



Design of a suspended germanium micro-antenna for efficient fiber-chip coupling in the long-wavelength mid-infrared range

A. SÁNCHEZ-POSTIGO,^{1,*} A. ORTEGA-MOÑUX,¹ D. PEREIRA-MARTÍN,¹ Í. MOLINA-FERNÁNDEZ,¹ R. HALIR,¹ P. CHEBEN,² J. SOLER PENADÉS,³ M. NEDELJKOVIC,³ G. Z. MASHANOVICH,³ J. G. WANGÜEMERT-PÉREZ¹

¹Universidad de Málaga, Dpto. Ingeniería de Comunicaciones, ETSI Telecomunicación, 29071 Málaga, Spain

²National Research Council Canada, 1200 Montreal Road, Bldg. M50, Ottawa K1A 0R6, Canada

³Optoelectronics Research Centre, University of Southampton, Southampton, SO17 1BJ, United Kingdom

*asp@ic.uma.es

Abstract: Recent developments of photonic integrated circuits for the mid-infrared band has opened up a new field of attractive applications for group IV photonics. Grating couplers, formed as diffractive structures on the chip surface, are key components for input and output coupling in integrated photonic platforms. While near-infrared optical fibers exhibit large mode field diameters compared to the wavelength, in the long-wave regime commercially available single-mode optical fibers have mode field diameters of the order of the operating wavelength. Consequently, an efficient fiber-chip surface coupler designed for the long-wave infrared range must radiate the power propagating in the waveguide with a higher radiation strength than a conventional grating coupler in the near-infrared range. In this article, we leverage the short electrical length required for long-wave infrared couplers to design a broadband all-dielectric micro-antenna for a suspended germanium platform at 7.67 μm . The design methodology is inspired by fundamental grating coupler equations, which remain valid even when the micro-antenna has only two or three diffractive elements. A simulated coupling efficiency of $\sim 40\%$ is achieved with a 1-dB bandwidth broader than 430 nm, which is almost twice the typical fractional bandwidth of a conventional grating coupler. In addition, the proposed design is markedly tolerant to fiber tilt misalignments of $\pm 10^\circ$. This all-dielectric micro-antenna design paves the way for efficient fiber-chip coupling in long-wavelength mid-infrared integrated platforms.

© 2019 Optical Society of America under the terms of the [OSA Open Access Publishing Agreement](#)

1. Introduction

While most research in group IV photonics has focused on the near-infrared (near-IR) region, important applications are emerging that are not limited to this band. Over the last decade, the mid-infrared (mid-IR) wavelength range, including the transparency windows of silicon and germanium [1–4], has attracted considerable attention. Molecules of many gases and liquids present characteristic vibrational absorption peaks in this spectral region. Potential applications include free-space atmospheric communications and biological, chemical and environmental absorption-based spectroscopy and sensing [5]. The availability of low-loss integrated waveguides and efficient fiber-chip couplers would enable the development of cost-effective and compact lab-on-chip systems [3].

Silicon-on-insulator (SOI) is the dominant platform for group IV photonics in the near-IR band [6]. However, for wavelengths above $\sim 4 \mu\text{m}$, the waveguide propagation loss due to intrinsic absorption of the buried oxide (BOX) becomes prohibitively large [1]. To circumvent this problem, several platforms based on dielectrics with low optical losses

beyond $\lambda \sim 4 \mu\text{m}$ have been proposed [7–15]. Another solution is the partial or total removal of the BOX, creating pedestal [16] or suspended waveguides [17–22]. We have demonstrated a suspended silicon platform with subwavelength grating (SWG) lateral cladding for wavelengths of $3.8 \mu\text{m}$ and $7.67 \mu\text{m}$ [19,20]. Germanium waveguides (low absorption loss up to $\sim 15 \mu\text{m}$) arise as a possible platform for the long-wave infrared (LWIR) range.

Research in LWIR integrated photonics has mainly focused on the development of low-loss waveguides, while other fundamental waveguide components are needed for practical implementations. In this context, fiber-chip edge couplers and grating couplers have been used to characterize new platforms (i.e. light coupling to measure propagation losses), but are not specifically optimized for high coupling efficiency. For example, in [23] a grating coupler was designed at $\lambda = 7.5 \mu\text{m}$ for the graded Ge-rich GeSi platform [15,24], with a comparatively low coupling efficiency of 6.3% (–12 dB) and a good 1-dB bandwidth of 300 nm. In [22], a 2D grating coupler was used at $\lambda \sim 7.67 \mu\text{m}$ for a suspended membrane Ge platform, but the coupler was not suspended and high SiO_2 loss is expected to compromise the coupling efficiency, albeit no data on its performance was reported. Alternatively, in [20] we utilized a conventional grating coupler for suspended silicon at $\lambda \sim 7.67 \mu\text{m}$ with coupling efficiency of 58% (–2.4 dB) and 1-dB bandwidth of 230 nm, but the coupler required a custom-made chalcogenide fiber with a mode field diameter of $29.5 \mu\text{m}$. Therefore, there is a need for a development of highly efficient fiber-chip couplers for standard (non-custom) fibers at LWIR wavelengths.

In the LWIR regime, chalcogenide single-mode optical fibers are commercially available, with high refractive index ($n_{\text{core}} \sim 2.7$) and large numerical aperture. In these fibers, a core diameter of the same order of magnitude as the operating wavelength is required to enable single-mode operation ($D_{\text{fiber}} \sim 12 \mu\text{m}$) [25–27]. As the optical properties of the chalcogenide fibers differ substantially from those of standard silica near-infrared optical fibers, new types of surface fiber-chip couplers need to be designed for the former. Here we propose a micro-antenna design for the suspended Ge platform with SWG lateral cladding (see Fig. 1). The micro-antenna exhibits a coupling efficiency of 40% (–4 dB) and a remarkable 1-dB bandwidth of 436 nm, which is a two-fold enhancement of the fractional bandwidth with respect to conventional grating couplers in the near-IR. At the same time, our device is robust to fiber misalignments of $\pm 10^\circ$ (which is approximately three-fold improvement over typical grating couplers in the near-IR) and tolerant to fabrication errors by up to $\Delta = \pm 150 \text{ nm}$ for transverse electric (TE) polarization at $\lambda \sim 7.67 \mu\text{m}$. The general strategy used to achieve these characteristics is to minimize the coupler length, specifically by radiating most of the power in the first diffractive elements, yielding the coupler length comparable to the operating wavelength. We show that fundamental grating coupler equations can still be used as a starting point for our design, even when, unlike in conventional grating couplers, the number of radiative elements is minimized. A 2D finite-difference time-domain (FDTD) simulation of the radiated field is shown in Fig. 1(b).

This article is organized as follows. In section 2, the suspended Ge waveguides with SWG lateral claddings are introduced. A basic theoretical framework for grating couplers and their particularities in the LWIR range is outlined in section 3. The micro-antenna design flow is presented in section 4. Simulation results (2D and 3D) are discussed in section 5, along with some further practical considerations, including the relation between the operating wavelength, the optical fiber parameters, the geometry of the coupler and the tolerance to fabrication and fiber alignment errors. Finally, conclusions are drawn in section 6.

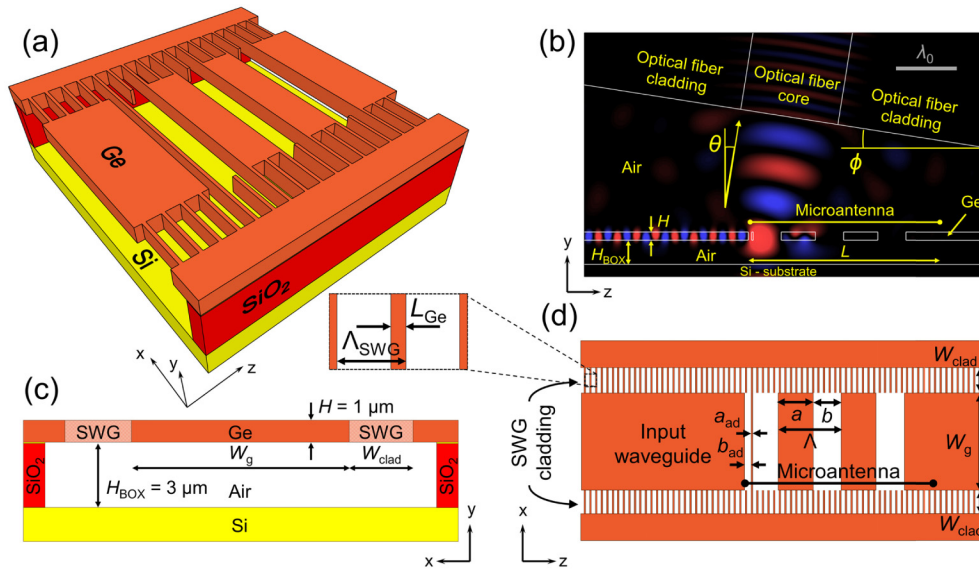


Fig. 1. Schematics of the microantenna fiber-chip coupler for the SWG-cladding suspended germanium platform. (a) 3D view, (b) side view, (c) front view and (d) top view. The side view schematics also shows the optical fiber (drawn to scale) and calculated (2D FDTD) propagation of the electric field (TE polarization, $\lambda = 7.67 \mu\text{m}$) coupled from the chip into the optical fiber. The microantenna comprises only three radiative elements (length Λ) and an adaptation section (length $a_{\text{ad}} + b_{\text{ad}}$). The total length of the microantenna, L , is comparable to the operating wavelength. While two radiation orders are allowed, most power is coupled to single order, which is clearly visible in the side view. Unlike in conventional grating couplers, most of the input power is radiated by the first radiative element.

2. Suspended germanium platform

Figure 1 shows 3D and 2D schematics of the micro-antenna implemented in the SWG-cladding suspended germanium waveguide platform, which is based on the Ge-on-SOI wafers described in [22]. The guiding layer thickness $H = 1 \mu\text{m}$ is chosen to assure vertical single-mode operation at the central wavelength of $7.67 \mu\text{m}$. At this wavelength, the Ge refractive index is $n_{\text{Ge}} \sim 4$.

To fabricate the waveguides, holes are fully etched into the Ge layer in the first step. Next, the structure is dipped into a hydrofluoric (HF) acid solution which removes the SiO₂ layer. This leaves the Ge waveguide core suspended and anchored to lateral germanium, by a periodic array of narrow Ge arms of length L_{Ge} . These strips constitute a SWG cladding of period Λ_{SWG} and width W_{clad} , performing a three-fold function: i) mechanically support the Ge waveguide core, ii) synthesize a cladding-core index contrast that enables light guiding for a fundamental mode and iii) allow the flow of the HF acid solution. The advantage of this SWG-cladding suspended platform is that it requires only one single dry etch step, unlike platforms based on suspended rib waveguides which require two etch steps, i.e. shallow etch for the waveguides and full etch for the venting holes [22]. In addition, the whole thickness of the Ge layer is used, thus making the structure more mechanically robust. Finally, the holes are in the close proximity to the waveguide core, minimizing the suspended area. This enables the realization of wide structures, such as MZI or MMI, as shown in suspended Si devices [19,20].

Following an approach similar to that in [20], we choose the SWG cladding with a synthesized refractive index of ~ 2 ($\Lambda_{\text{SWG}} = 1 \mu\text{m}$, $L_{\text{Ge}} = 0.2 \mu\text{m}$), and $W_{\text{clad}} = 3 \mu\text{m}$.

3. Grating couplers in the mid-IR band

3.1. Fundamentals

A surface grating coupler (SGC) is a diffractive structure formed in a planar waveguide, which couples the waveguide mode to an off-chip plane wave. The field radiated upwards is typically intercepted by an optical fiber positioned above the grating at a specific angle. As an alternative to edge couplers [28,29], SGCs enable wafer-scale testing and benefit from a high tolerance to alignment errors while obviating the need for cleaving or polishing the chip facets [30].

Surface grating coupler radiation is governed by the grating momentum conservation equation [31]:

$$n_a \sin \theta_m = n_B + m \frac{\lambda}{\Lambda}, \quad (1)$$

where n_a is the refractive index of the medium into which light is radiated, m is a diffraction order, θ_m is the radiation angle for a given diffraction order, Λ is the grating period, λ is the wavelength, and n_B is the effective index of the Bloch-Floquet leaky mode supported by the periodic waveguide.

SGCs main performance metrics are the coupling efficiency (CE), the back-reflections (R) and the operational bandwidth (BW). Coupling efficiency is defined as the fraction of input power that is coupled from the chip to the optical fiber and vice versa. To achieve the maximum value of CE (100%), all injected power must be radiated upwards with a field profile that perfectly matches that of the near Gaussian mode of the optical fiber. Nevertheless, in uniformly periodic grating couplers, the radiated field follows an exponential profile with a decay constant proportional to grating radiation strength. Thus, to maximize the overlap for a given fiber (up to the theoretical maximum of $\sim 80\%$ for the exponential-to-Gaussian overlap [30]), a specific grating radiation strength is required. Coupling efficiency also depends on back-reflections, arising from the intrinsic reflectivity of the grating, its mode mismatch with the uniform input waveguide and the Fresnel loss at the air-fiber interface. Typically, back-reflections smaller than -20 dB are required [32]. Grating coupler bandwidth (typically measured at 1 dB) is limited by the radiation angle change with the operating wavelength, according to Eq. (1). The bandwidth is determined by geometry and material refractive indices, but also by the mode field diameter and the numerical aperture of the optical fiber [33–35]. Typical near-IR grating couplers at $\lambda \sim 1.55 \mu\text{m}$ have BW of ~ 50 nm [33], which corresponds to a fractional bandwidth $BW/\lambda = 3.23\%$. In consequence, to maintain the same fractional bandwidth, BW of at least ~ 250 nm is required at $\lambda = 7.67 \mu\text{m}$, in accordance with Maxwell's equations scaling properties [36].

Light can be radiated by the grating in various diffraction orders, each radiating at a different angle, as in Eq. (1). Since the optical fiber can only be aligned to collect light from one order, grating couplers are usually designed with pitch Λ that meets Eq. (1) for only one diffraction order, which is typically $m = -1$ [31]. For some applications, gratings can also be designed to fulfill the single-beam radiation condition for the diffraction order $m = -2$ [23,37,38].

However, theoretically, high coupling efficiency can still be achieved when several orders are supported, provided the grating is designed such that most of the optical power is radiated into a single order. In this work, we relax the single-beam constraint and show that good designs can be achieved with two supported diffraction orders ($m = -2$ and $m = -3$) when power is coupled to only one of them (in our case, $m = -2$). From Eq. (1) it follows that no more than two orders will be radiated if

$$\Lambda < \frac{\lambda}{n_a}. \quad (2)$$

This bound can be used to define the pitch range to be explored in the design process.

3.2 Fiber-chip surface couplers in the LWIR

A limited number of off-the-shelf (non-custom) single-mode optical fibers is commercially available for the LWIR band [25–27]. These optical fibers have different properties compared to near-IR fibers, with various implications affecting the design and performance of surface couplers, such as:

High refractive index of the fiber core. The core material of LWIR fibers, arsenic triselenide (As_2Se_3), is transparent in the mid-IR and has a refractive index of ~ 2.7 [26]. This value is almost twice the refractive index of near-IR fiber cores, which results in increased Fresnel reflections at the optical fiber facet. Therefore, an index-matching gel should be used in the gap between the chip and the fiber facet [39]. If this is not possible, the optical fiber must be accurately positioned in the y direction (see Fig. 1) to collect the highest possible power, but this may increase back-reflections.

Small mode field diameter (MFD). The MFD -to-wavelength ratio ($MFD_\lambda = MFD/\lambda$) for LWIR fibers is much smaller than for conventional near-IR fibers. For example, IRFlex IRF-Se-12 fiber has a core diameter $D_{\text{core}} = 12 \mu\text{m}$ and a numerical aperture $NA = 0.47$ [26]. According to the Marcuse's formula [40], these fiber specifications yield $MFD_\lambda \sim 1.8$ at $\lambda = 7.67 \mu\text{m}$. This MFD_λ value is much lower than for a conventional SMF-28 fiber at $\lambda = 1.55 \mu\text{m}$, which has $MFD_\lambda \sim 6.7$ [41]. As the size of the coupling structure is in close relation to the mode field diameter of the fiber, the optimum electrical length of the grating, $L_\lambda = L/\lambda$ [42], will be about 4 times shorter at $\lambda = 7.67 \mu\text{m}$ than at $\lambda = 1.55 \mu\text{m}$. Accordingly, a grating with a substantially higher radiation strength will be required and coupler designs will be more complex than simply scaling up the coupler geometry from near-IR to LWIR. The shorter electrical length also implies a narrow diverging outgoing beam with cylindrical wavefront. Since grating couplers in the near-IR typically require about 20 periods to efficiently couple light into an optical fiber [30], an efficient LWIR coupler would require only $\sim 20/4 \sim 5$ periods, assuming the pitch Λ is scaled correspondingly. If Λ is increased, the number of periods can be even smaller. Due to these fundamental differences with near-IR surface couplers, it can be argued that efficient LWIR surface couplers for non-custom optical fibers should operate more like micro-antennas rather than conventional grating couplers.

Beside the considerations related to optical fibers, the coupler design for the LWIR is also affected by the specific materials choice. As intrinsic silicon loss becomes high for $\lambda > 8 \mu\text{m}$, other materials are required for this wavelength range, for example, germanium ($n_{\text{Ge}} \sim 4$), in a suspended waveguide platform. As the latter provides a higher index contrast than SOI and the Bragg band gap in periodic structures increases with the index contrast [36], the range of Λ values within the Bragg regime is increased for germanium gratings compared to silicon gratings ($\epsilon_{\text{Ge}} = n_{\text{Ge}}^2 \sim 16 > \epsilon_{\text{Si}} = n_{\text{Si}}^2 \sim 12$). This results in radiation zones with a reduced range of periods Λ . Most single-beam grating couplers operate in the first radiation zone, located between first- and second-order Bragg regimes [31]. Designs operating in this radiation zone can suffer from narrower bandwidth and reduced tolerance to fabrication imperfections. To circumvent these limitations, different radiation zones should be examined when designing Ge-based fiber-chip surface couplers.

4. Design

Despite the small number of diffractive elements in the proposed micro-antenna, the grating coupler equation and typical design strategies can still be used, as will be shown in this section. The micro-antenna is designed according to a 2D model shown in Fig. 1(b), assuming the structure is invariant with x . We use our in-house 2D Fourier eigenmode expansion

method (Fourier-EEM) simulator, FEXEN, which is optimized for fast and efficient analysis of periodic structures [43]. The optimization of the pitch and the duty cycle is summarized in the following steps:

- i) Values of Λ and DC that produce fabricable structures with low back-reflections and operating far from Bragg regimes are selected. At this step, the calculations are performed efficiently with FEXEN by exciting only one period with the fundamental mode field of a homogeneous waveguide and imposing Bloch-Floquet boundary conditions on the other side, thus emulating a semi-infinite periodic structure.
- ii) For the selected structures with comparatively low back-reflections, coupling efficiency and radiation angle are estimated from the radiated field and power. The simulations are carried out with FEXEN, now including the complete structure within the simulation window (input homogeneous waveguide, micro-antenna with enough number of periods to radiate most input power, and output homogeneous waveguide).
- iii) The best design is selected according to three figures of merit: high coupling efficiency, small radiation angle and high tolerance to fabrication imperfections.
- iv) For the best design, back-reflections are further reduced with an adaptation section placed between the input access waveguide and the first radiative element.

Once the optimal values for Λ and DC are found, the structure is simulated with 2D and 3D FDTD.

Back-reflections (R) are calculated for a complete set of (Λ, DC) pairs, which constitute our search space. Figure 2 shows the map of back-reflections for all possible gratings with periods ranging from 1 μm up to 10 μm . Below $\Lambda \sim 1 \mu\text{m}$, the periodic waveguide is working in the subwavelength grating (SWG) regime, i.e. neither radiation nor Bragg reflections take place [44,45]. The upper bound for Λ was chosen to cover all periods that meet Eq. (2), $\Lambda < \lambda = 7.67 \mu\text{m}$. Since good designs could still be found for longer periods, additional values (up to $\Lambda = 10 \mu\text{m}$) were also evaluated. Bragg and radiation regimes can be recognized visually in this contour map of R . Reddish areas where $R > 70\%$ correspond to the different Bragg regimes. On the other hand, dark blue areas with $R \leq 30\%$, delimited with solid lines in Fig. 2, are candidates for good coupler designs. We have chosen the maximum acceptable value of 30% because, as we will discuss later, back-reflections of this magnitude can be easily suppressed using simple adaptation sections. However, not all zones with low back-reflections are useful in practice. Those with high DC values, i.e. small hole sizes, could prevent HF from successfully removing the BOX beneath the wide micro-antenna, while those with low DC values, i.e. thin germanium strips, could compromise the mechanical stability of the suspended coupler. Based on our previous suspended silicon devices [20], structures with strips narrower than $a = 200 \text{ nm}$ and holes smaller than $b = 500 \text{ nm}$ are prone to collapsing or remaining unsuspended. Furthermore, designs located in narrow zones between two Bragg regions can exhibit low tolerance to fabrication errors, as small variations in Λ or DC can translate into huge variations in the radiation angle or can push the working point into the Bragg regime, leading to excessive back-reflections and hence low coupling efficiency. With all of these considerations taken into account, we have finally designated seven regions of interest (ROIs), labeled with numbers in Fig. 2, which can potentially contain the best possible designs. It is important to remark that most of these ROIs (3 – 7) do not meet single beam condition [31,37], and therefore they would not be evaluated following a conventional grating coupler design approach.

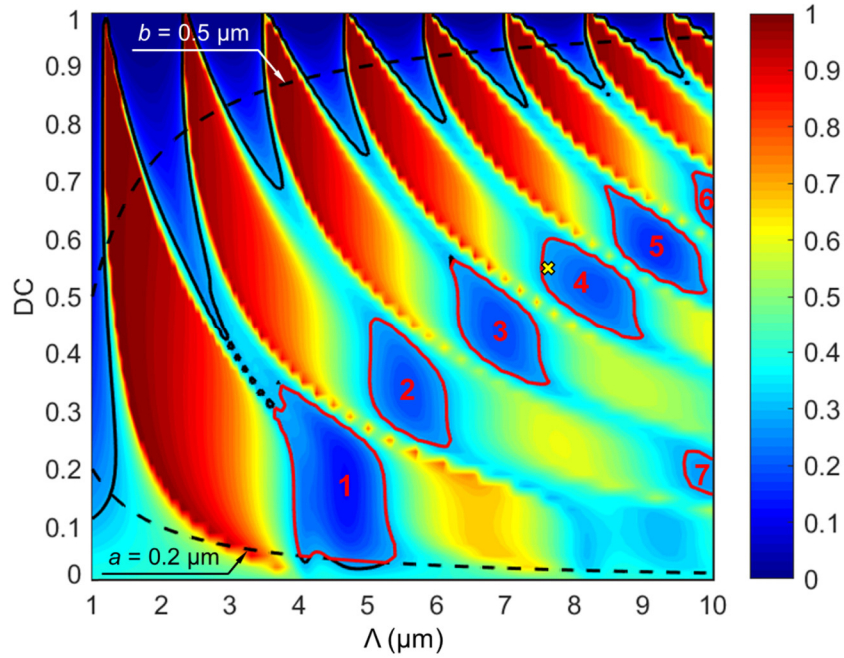


Fig. 2. Simulated back-reflections (R) as a function of the pitch (Λ) and duty cycle (DC). Areas with $R \leq 30\%$ are delimited with solid lines. Unpractical zones due to fabrication restrictions are demarcated with dashed curves. Regions of interest (feasible gratings, with low back-reflections and operating far enough from Bragg regimes) are labeled with numbers and enclosed in red lines. Final design point is marked with a yellow cross.

Coupling efficiency and radiation angle are estimated exclusively for the reduced parameter space determined by the ROIs. For a mode field diameter of $13.56 \mu\text{m}$, the structures with highest CE values can be found in ROIs 3 (bottom part), 4 and 7, as shown in Fig. 3(a). Nonetheless, we discard designs in ROIs 3 and 7, as their associated radiation angles are greater than the maximum value accepted by typical measurement set-ups, about 30° [see Figs. 3(b) and 3(c)]. In ROI 4, we choose the design with $\Lambda = 7.6 \mu\text{m}$ and $DC = 0.55$, resulting in a coupling efficiency $CE = 0.29$ with a radiation angle of $\theta \sim 9^\circ$. Despite its proximity to the ROI edge, this design is tolerant to fabrication imperfections, as typical errors ($\pm 150 \text{ nm}$) do not push the structure outside the ROI. Since this design is located between the fourth- and fifth-order Bragg regimes (fourth radiation zone), in general it could support up to four radiation orders simultaneously ($m = -1, -2, -3$ and -4). However, as $\Lambda < \lambda$, i.e. Equation (2) is satisfied, only two orders can be excited. Specifically, for the effective index calculated by our in-house simulator ($n_B = 2.18$), the orders that meet Eq. (1) are $m = -2$ and $m = -3$. This is, to the best of our knowledge, the first time a surface chip-fiber coupler is designed to operate with high-order diffraction beams in the fourth radiation zone.

To reduce back-reflections, an adaptation section comprising an air trench and a germanium strip of lengths b_{ad} and a_{ad} , respectively, is introduced in front of the first diffractive element, as schematized in Fig. 1(d). Both lengths, $b_{ad} = 400 \text{ nm}$ and $a_{ad} = 200 \text{ nm}$, are chosen to minimize back-reflections down to $R < 0.2\%$ (around -30 dB). As a result of the enhanced matching between the waveguide and the grating region, the amount of power radiated upwards is increased, yielding a coupling efficiency of ~ 0.4 .

The final geometric parameters are summarized in Table 1.

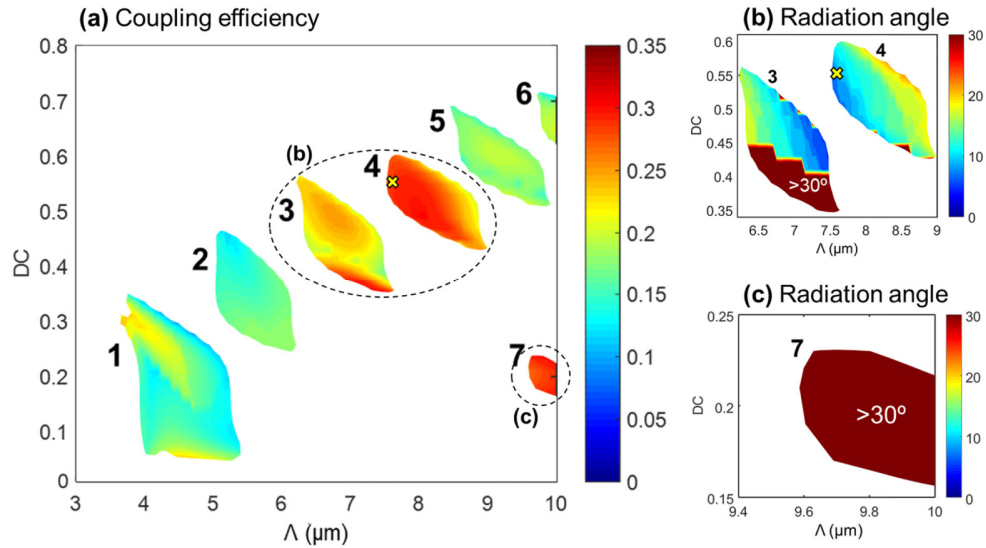


Fig. 3. (a) Simulated coupling efficiency (CE) and (b), (c) absolute value of the simulated radiation angle ($|\theta|$) as a function of the pitch (Λ) and duty cycle (DC) for designs contained in the ROIs delimited in Fig. 2. The final design point is marked with a yellow cross.

Table 1. Final geometry of the designed micro-antenna at $\lambda = 7.67 \mu\text{m}$

Λ (μm)	DC	a (μm)	b (μm)	a_{ad} (μm)	b_{ad} (μm)
7.6	0.55	4.18	3.42	0.2	0.4

5. Simulation results and discussion

Once the micro-antenna is designed with 2D Fourier-EEM, we analyze it with 2D FDTD using RSoft FullWAVE by Synopsys. Figure 4(a) shows the simulated electric field distribution when the fundamental TE mode of the input waveguide is excited from the left. Because of the high radiation strength, most of the input power is radiated in the first radiative element and the wavefront is cylindrical instead of being flat. Furthermore, only one radiated beam ($\theta \sim 9^\circ$) can be seen in Fig. 4(a), despite the coupler working in the fourth radiation ROI according to Figs. 2 and 3. For an infinitely periodic waveguide with the designed Λ and DC , our in-house simulator returns a Floquet-Bloch effective index $n_B = 2.18$, which, from Eq. (1), implies $\theta_2 = \arcsin(0.16) = 9.2^\circ$, in good agreement with the angle shown in Fig. 4(a). Likewise, this analysis is confirmed with the far-field radiation pattern we calculated with the FullWAVE tool from a near-field cut 500 nm above the chip plane. The diagram shows that two radiation orders are supported, and one of them ($\theta = 8.6^\circ \sim \theta_2$) noticeably prevails over the other ($\theta = -63.6^\circ$). The predominant radiation angle predicted by this far-field approximation confirms the inclination of the fiber estimated from our 2D Fourier-EEM simulations. Also, as a consequence of the strong exponential decay, the full width at half maximum of the fundamental beam is $FWHM \sim 25^\circ$, more than twice that of conventional grating couplers with comparable coupling efficiency in the near-IR [46]. The simulation of the micro-antenna with $H_{\text{BOX}} \rightarrow \infty$ [see Fig. 4(b)] shows that the radiation angle is mainly determined by the periodic structure, with marginal influence of the 3-μm thick BOX. We observe that the silicon substrate acts as a bottom reflector, increasing the directionality from 50% to 62% and decreasing the $FWHM$ from 38° to 25° .

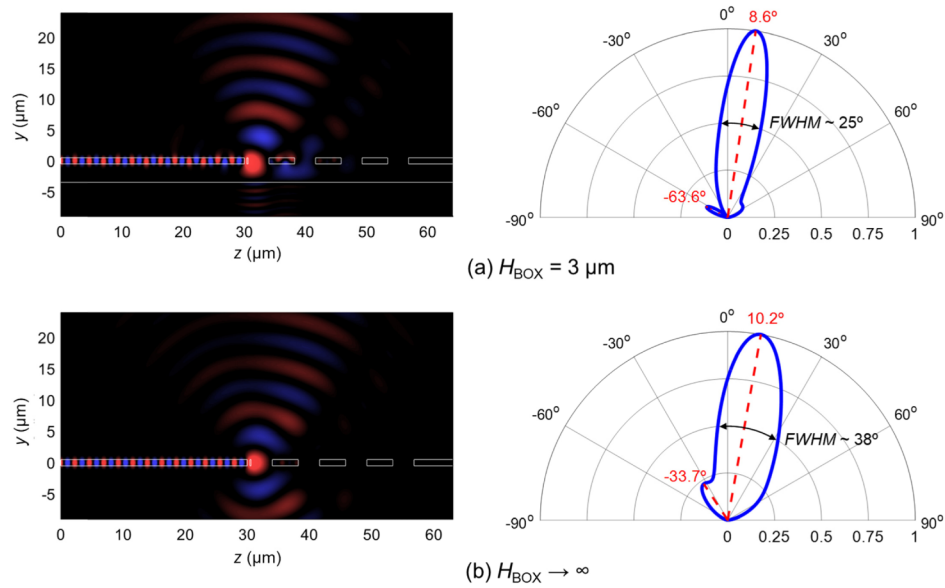


Fig. 4. 2D FDTD propagation of the electric field (TE polarization) and far-field radiation pattern (normalized intensity) derived from a field cut at $y = 500$ nm above the grating surface when (a) $H_{\text{BOX}} = 3 \mu\text{m}$ and (b) $H_{\text{BOX}} \rightarrow \infty$. Only one radiated beam is observable. In these simulations the optical fiber has not yet been included. The input waveguide, micro-antenna with three radiative elements, and output waveguide are outlined in the FDTD propagations. The silicon substrate is also outlined in (a).

A 2D slab model of an IRFlex IRF-Se-12 optical fiber is now introduced in the simulation window (core diameter $D_{\text{core}} = 12 \mu\text{m}$, cladding diameter $D_{\text{clad}} = 170 \mu\text{m}$, core refractive index $n_{\text{core}} = 2.7$ and cladding refractive index $n_{\text{clad}} = 2.658$ [26]). As the micro-antenna radiation angle is $\theta \sim 9^\circ$, the fiber is tilted $\phi = 9^\circ$ with respect to the vertical. Since reflections at the fiber facet can compromise the coupling efficiency, the height of the fiber above the chip must be chosen carefully to maximize coupling efficiency, unless an index-matching gel is used. Note that these reflections would affect not only the proposed micro-antenna, but any fiber-chip coupler. Figure 5 shows the simulated coupling efficiency as a function of the fiber-chip distance d_{fiber} . We observe a standing wave pattern in the air gap between the micro-antenna and the fiber. The distance between maxima is approximately $\lambda/2 \sim 3.8 \mu\text{m}$. In practice, this separation provides enough margin to accurately align an optical fiber using nanopositioning stages. Hereafter in our simulations we select $d_{\text{fiber}} = 14.46 \mu\text{m}$ (central maximum in Fig. 5) because it is the minimum value of d_{fiber} that could be used maintaining clearance between chip surface and fiber cladding.

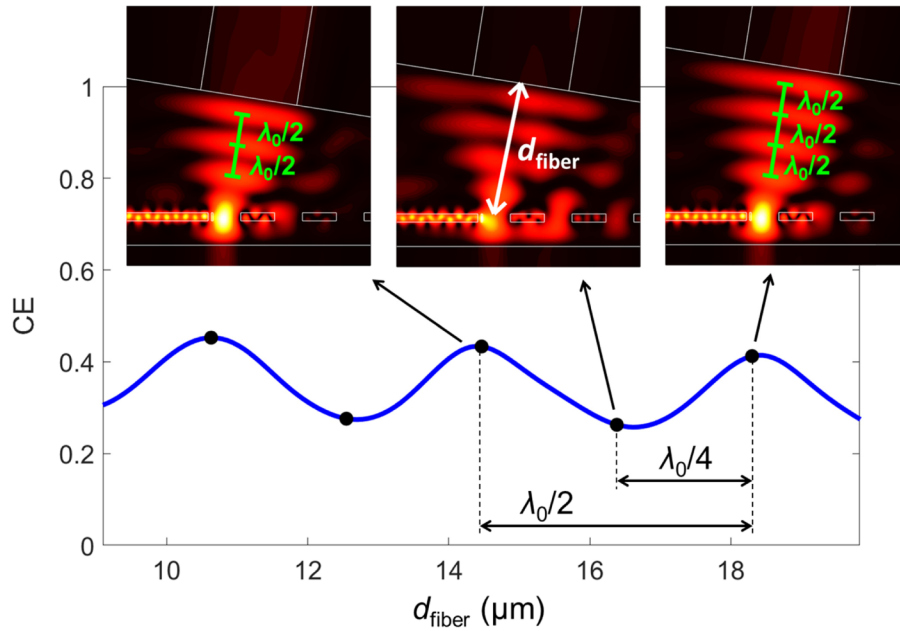


Fig. 5. Simulated coupling efficiency as a function of distance d_{fiber} of the optical fiber with respect to the chip plane. A standing wave pattern is formed in the air gap between the grating and the fiber, with a distance between consecutive maxima or minima of $\sim \lambda/2$. Magnitudes of the electric field (TE polarization) are also included for several points.

Table 2 provides the coupling efficiency, back-reflections and non-coupled transmitted power to the output waveguide for several micro-antennas with a different number (N) of diffractive elements. These parameters are calculated with FullWAVE by monitoring the field inside the optical fiber, the input waveguide and the output waveguide and computing the overlap with the corresponding mode fields. The 2D FDTD field distribution of each micro-antenna is shown in Fig. 6. As transmitted power drops from $T = 32.6\%$ ($N = 1$) to 2.4% ($N = 2$), it is apparent that most of the power is radiated in the first two radiative elements, the first one being the strongest. For $N > 2$, micro-antenna performances are virtually indistinguishable. From now on we choose $N = 3$ for our nominal micro-antenna design since larger number of periods do not result in significant improvements. The simulated coupling efficiency is $CE = 0.43$, in good agreement with the value estimated without the optical fiber during the design process. Reflections at the input waveguide are $R < 5\%$, higher than those initially designed due to the reflections at the air-fiber interface.

Table 2. Simulated coupling efficiency (CE), back-reflections (R) and transmitted power to the output waveguide (T) for the designed micro-antenna as a function of the number of diffractive elements (N)

N	CE (%)	R (%)	T (%)
1	16	0.31	32.59
2	40	4.10	2.40
3	43	4.65	0.48
4	43	4.54	0.14

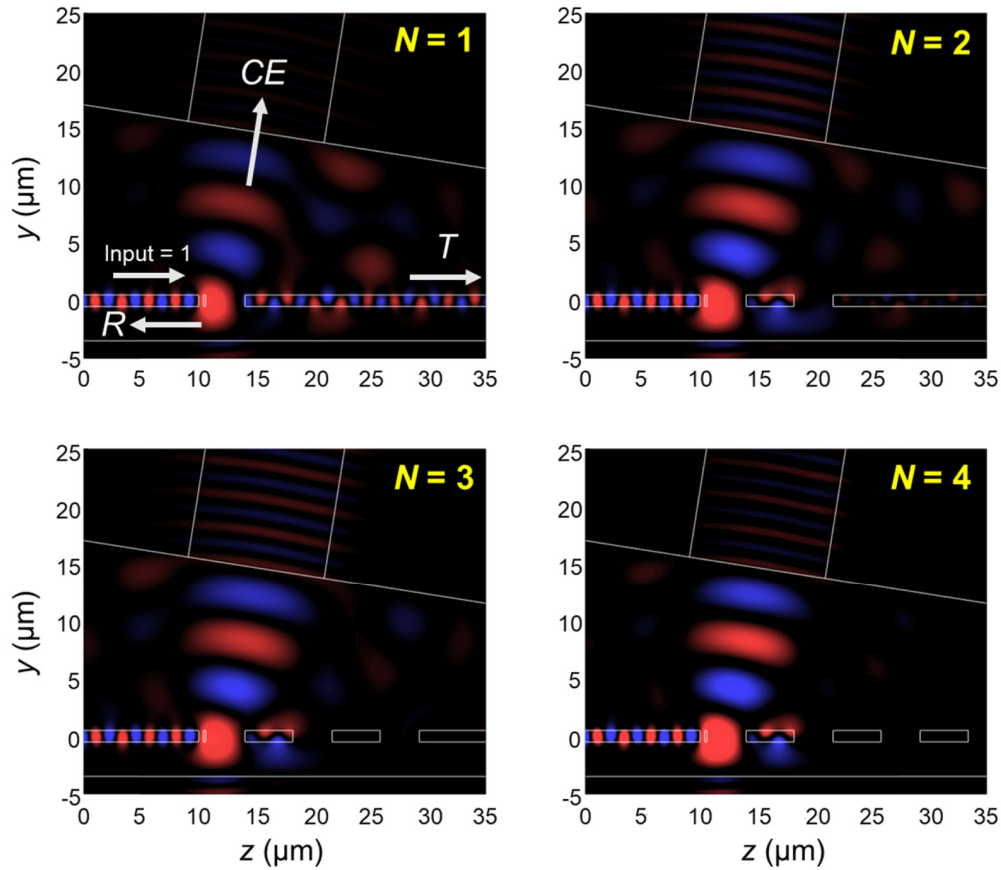


Fig. 6. Influence of the number of periods N on the radiation of the micro-antenna. 2D FDTD propagations of the electric field (TE polarization) are calculated with the fiber included in the simulation window. Device geometry and optical fiber are outlined.

The coupling efficiency as a function of the wavelength is shown in Fig. 7(a) (blue line). The simulation of the reciprocal case, i.e. coupling light from the fiber into the chip, resulted in the same efficiency in virtue of the reciprocity principle [47]. A 1-dB bandwidth of $BW = 465$ nm is achieved. This corresponds to a fractional bandwidth $BW/\lambda = 6.06\%$, which is almost twice the ratio of standard grating couplers at $\lambda = 1.55$ μm ($BW/\lambda = 3.23\%$ assuming $BW = 50$ nm) [33]. Such a broad bandwidth was anticipated because the micro-antenna has been designed to efficiently couple light to an optical fiber with reduced core width and large numerical aperture [33,34]. Additionally, Fig. 7(b) represents the coupling efficiency as a function of the fiber angle misalignments ($\Delta\phi = \phi - 9^\circ$). The coupling efficiency is very tolerant to fiber tilt, with a 1-dB angular bandwidth of 19.3° (about $\pm 10^\circ$ with respect to the nominal tilt angle of 9°), which approximately constitutes a three-fold enhancement compared to the angular bandwidth of conventional grating couplers in the near-IR (around $\pm 3^\circ$) [48]. This improvement arises from the broad angular width of the outgoing beam (see Fig. 4) and is consistent with the broad 1-dB bandwidth shown in Fig. 7(a).

The proposed micro-antenna is very robust against fabrication errors. Figure 7(a) shows the calculated coupling efficiency when a deviation $\Delta = \pm 150$ nm is introduced in the length of the Ge segments a and a_{ad} [see Fig. 1(b)]. The penalty in coupling efficiency, maintaining the same fiber tilt angle as in the nominal case (i.e. 9°), is less than 10% at the central wavelength. The reason is that the absolute error $\Delta = \pm 150$ nm (a typical value for our fabrication process) corresponds to a relative error $\Delta DC \sim 2\%$ due to the large pitch.

Finally, 3D FDTD simulations are carried out to double-check the design. The width of the micro-antenna, which was not needed for the 2D approximation, was chosen to maximize the overlap between the radiated field and the optical fiber mode in the fiber facet plane, resulting in $W_g \sim 20 \mu\text{m}$. Figure 7(a) (blue dashed line) depicts the coupling efficiency as a function of the wavelength, yielding $CE = 39.6\%$ and $BW = 436 \text{ nm}$. Figure 7(b) shows an angular bandwidth of 19.6° . These results agree well with our 2D simulations.

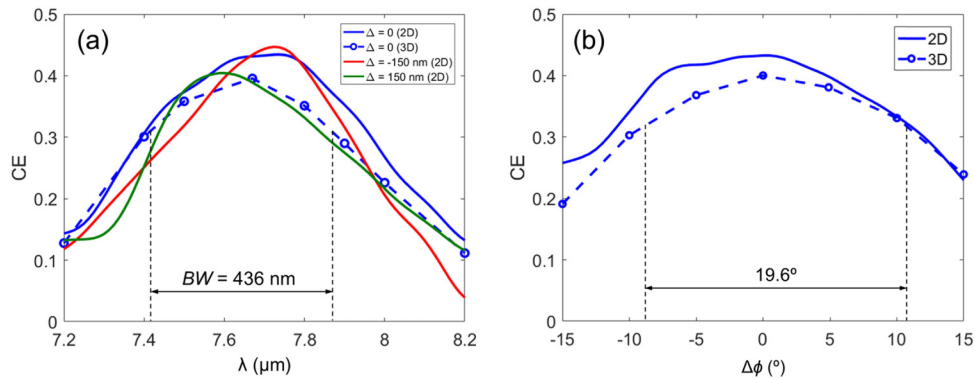


Fig. 7. (a) Simulated coupling efficiency (CE) as a function of the wavelength when dimension errors $\Delta = 0$ (blue line), 150 nm (green line) and -150 nm (red line) affect the length of the germanium strips of the structure. 3D FDTD simulation results are also included (blue dashed line) for the nominal design. The radiation angle is $\theta = 9^\circ$ in all cases. (b) Simulated coupling efficiency (CE) as a function of fiber tilt misaligned angle $\Delta\phi$.

6. Conclusions

The characteristic parameters of integrated platforms and commercial optical fibers complicate the design of surface fiber-chip couplers in the long wave IR regime (LWIR). In this work we have proposed a new all-dielectric micro-antenna design for a suspended germanium platform at the LWIR wavelength of $7.67 \mu\text{m}$. A coupling efficiency of $\sim 40\%$ (-4 dB) is predicted with reduced back reflections and a broad 1-dB bandwidth greater than 430 nm , which almost doubles the typical fractional bandwidth of a conventional grating coupler in the near-infrared. An excellent angular bandwidth of $\sim 20^\circ$ is also achieved, providing for a fiber tilt tolerance of $\pm 10^\circ$ with an efficiency penalty of only 1 dB . Moreover, coupling efficiency is tolerant to fabrication errors up to $\pm 150 \text{ nm}$. These results constitute the first step for the development of a platform for suspended Ge waveguides and building blocks with lateral SWG cladding in the LWIR band. We furthermore believe that the micro-antenna approach can be readily extended to other long-wave platforms.

Funding

Spanish Ministerio de Ciencia, Innovación y Universidades, Programa Estatal de Investigación, Desarrollo e Innovación Orientada a los Retos de la Sociedad (cofinanciado FEDER) (TEC2016-80718-R); Spanish Ministerio de Ciencia, Innovación y Universidades, Programa Estatal de Promoción del Talento y su Empleabilidad en Investigación, Desarrollo e Innovación (FPU14/06121, FPU17/00638); Universidad de Málaga.

References

1. R. Soref, "Mid-infrared photonics in silicon and germanium," *Nat. Photonics* **4**(8), 495–497 (2010).
2. G. Z. Mashanovich, M. Nedeljkovic, J. Soler-Penades, Z. Qu, W. Cao, A. Osman, Y. Wu, C. J. Stirling, Y. Qi, Y. X. Cheng, L. Reid, C. G. Littlejohns, J. Kang, Z. Zhao, M. Takenaka, T. Li, Z. Zhou, F. Y. Gardes, D. J. Thomson, and G. T. Reed, "Group IV mid-infrared photonics [Invited]," *Opt. Mater. Express* **8**(8), 2276–2286 (2018).
3. T. Hu, B. Dong, X. Luo, T.-Y. Liow, J. Song, C. Lee, and G.-Q. Lo, "Silicon photonic platforms for mid-infrared applications [Invited]," *Photon. Res.* **5**(5), 417–430 (2017).

4. D. Marris-Morini, V. Vakarin, J. M. Ramirez, Q. Liu, A. Ballabio, J. Frigerio, M. Montesinos, C. Alonso-Ramos, X. Le Roux, S. Serna, D. Benedikovic, D. Chrastina, L. Vivien, and G. Isella, "Germanium-based integrated photonics from near- to mid-infrared applications," *Nanophotonics* **7**(11), 1781–1793 (2018).
5. R. A. Soref, S. J. Emelett, and W. R. Buchwald, "Silicon waveguided components for the long-wave infrared region," *J. Opt. A, Pure Appl. Opt.* **8**(10), 840–848 (2006).
6. X. Chen, M. M. Milosevic, S. Stankovic, S. Reynolds, T. D. Bucio, K. Li, D. J. Thomson, F. Gardes, and G. T. Reed, "The emergence of silicon photonics as a flexible technology platform," *Proc. IEEE* **106**(12), 2101–2116 (2018).
7. T. Baehr-Jones, A. Spott, R. Ilic, A. Spott, B. Penkov, W. Asher, and M. Hochberg, "Silicon-on-sapphire integrated waveguides for the mid-infrared," *Opt. Express* **18**(12), 12127–12135 (2010).
8. Y. Yue, L. Zhang, H. Huang, R. G. Beausoleil, and A. E. Willner, "Silicon-on-nitride waveguide with ultralow dispersion over an octave-spanning mid-infrared wavelength range," *IEEE Photonics J.* **4**(1), 126–132 (2012).
9. B. Dong, X. Luo, S. Zhu, M. Li, D. Hasan, L. Zhang, S. J. Chua, J. Wei, Y. Chang, G.-Q. Lo, K. W. Ang, D.-L. Kwong, and C. Lee, "Aluminum nitride on insulator (AlNOI) platform for mid-infrared photonics," *Opt. Lett.* **44**(1), 73–76 (2019).
10. A. Malik, M. Muneeb, S. Pathak, Y. Shimura, J. Van Campenhout, R. Loo, and G. Roelkens, "Germanium-on-silicon mid-infrared arrayed waveguide grating multiplexers," *IEEE Photonics Technol. Lett.* **25**(18), 1805–1808 (2013).
11. C. Alonso-Ramos, M. Nedeljkovic, D. Benedikovic, J. S. Penadés, C. G. Littlejohns, A. Z. Khokhar, D. Pérez-Galacho, L. Vivien, P. Cheben, and G. Z. Mashanovich, "Germanium-on-silicon mid-infrared grating couplers with low-reflectivity inverse taper excitation," *Opt. Lett.* **41**(18), 4324–4327 (2016).
12. M. Nedeljkovic, J. S. Penades, V. Mittal, G. S. Murugan, A. Z. Khokhar, C. Littlejohns, L. G. Carpenter, C. B. E. Gawith, J. S. Wilkinson, and G. Z. Mashanovich, "Germanium-on-silicon waveguides operating at mid-infrared wavelengths up to 8.5 μm ," *Opt. Express* **25**(22), 27431–27441 (2017).
13. W. Li, P. Anantha, S. Bao, K. H. Lee, X. Guo, T. Hu, L. Zhang, H. Wang, R. Soref, and C. S. Tan, "Germanium-on-silicon nitride waveguides for mid-infrared integrated photonics," *Appl. Phys. Lett.* **109**(24), 241101 (2016).
14. J. M. Ramirez, V. Vakarin, C. Gilles, J. Frigerio, A. Ballabio, P. Chaisakul, X. L. Roux, C. Alonso-Ramos, G. Maisons, L. Vivien, M. Carras, G. Isella, and D. Marris-Morini, "Low-loss Ge-rich $\text{Si}_{0.2}\text{Ge}_{0.8}$ waveguides for mid-infrared photonics," *Opt. Lett.* **42**(1), 105–108 (2017).
15. J. M. Ramirez, Q. Liu, V. Vakarin, J. Frigerio, A. Ballabio, X. Le Roux, D. Bouville, L. Vivien, G. Isella, and D. Marris-Morini, "Graded SiGe waveguides with broadband low-loss propagation in the mid infrared," *Opt. Express* **26**(2), 870–877 (2018).
16. P. T. Lin, V. Singh, Y. Cai, L. C. Kimerling, and A. Agarwal, "Air-clad silicon pedestal structures for broadband mid-infrared microphotonics," *Opt. Lett.* **38**(7), 1031–1033 (2013).
17. J. Chiles, S. Khan, J. Ma, and S. Fathpour, "High-contrast, all-silicon waveguiding platform for ultra-broadband mid-infrared photonics," *Appl. Phys. Lett.* **103**(15), 151106 (2013).
18. Z. Cheng, X. Chen, C. Y. Wong, K. Xu, and H. K. Tsang, "Mid-infrared suspended membrane waveguide and ring resonator on silicon-on-insulator," *IEEE Photonics J.* **4**(5), 1510–1519 (2012).
19. J. S. Penades, A. Ortega-Moñux, M. Nedeljkovic, J. G. Wangüemert-Pérez, R. Halir, A. Z. Khokhar, C. Alonso-Ramos, Z. Qu, I. Molina-Fernández, P. Cheben, and G. Z. Mashanovich, "Suspended silicon mid-infrared waveguide devices with subwavelength grating metamaterial cladding," *Opt. Express* **24**(20), 22908–22916 (2016).
20. J. S. Penadés, A. Sánchez-Postigo, M. Nedeljkovic, A. Ortega-Moñux, J. G. Wangüemert-Pérez, Y. Xu, R. Halir, Z. Qu, A. Z. Khokhar, A. Osman, W. Cao, C. G. Littlejohns, P. Cheben, I. Molina-Fernández, and G. Z. Mashanovich, "Suspended silicon waveguides for long-wave infrared wavelengths," *Opt. Lett.* **43**(4), 795–798 (2018).
21. J. Kang, Z. Cheng, W. Zhou, T.-H. Xiao, K.-L. Gopalakrishna, M. Takenaka, H. K. Tsang, and K. Goda, "Focusing subwavelength grating coupler for mid-infrared suspended membrane germanium waveguides," *Opt. Lett.* **42**(11), 2094–2097 (2017).
22. A. Osman, M. Nedeljkovic, J. Soler Penades, Y. Wu, Z. Qu, A. Z. Khokhar, K. Debnath, and G. Z. Mashanovich, "Suspended low-loss germanium waveguides for the longwave infrared," *Opt. Lett.* **43**(24), 5997–6000 (2018).
23. Q. Liu, J. M. Ramirez, V. Vakarin, D. Benedikovic, C. Alonso-Ramos, J. Frigerio, A. Ballabio, G. Isella, L. Vivien, and D. Marris-Morini, "7.5 μm wavelength fiber-chip grating couplers for Ge-rich SiGe photonics integrated circuits," in *Silicon Photonics: From Fundamental Research to Manufacturing*, R. G. Baets, P. O'Brien, and L. Vivien, eds. (SPIE, 2018), p. 23.
24. J. M. Ramirez, V. Vakarin, C. Gilles, J. Frigerio, A. Ballabio, P. Chaisakul, X. L. Roux, C. Alonso-Ramos, G. Maisons, L. Vivien, M. Carras, G. Isella, and D. Marris-Morini, "Low-loss Ge-rich $\text{Si}_{0.2}\text{Ge}_{0.8}$ waveguides for mid-infrared photonics," *Opt. Lett.* **42**(1), 105–108 (2017).
25. "CorActive - Select Cutoff Singlemode Fiber," <http://coractive.com/products/mid-ir-fibers-lasers/select-cutoff-singlemode-fiber/index.html>.
26. "Infrared Fiber Optics | IRFlex Corporation," <https://www.irflex.com/products/irf-se-series/>.
27. C. Caillaud, C. Gilles, L. Provino, L. Brilland, T. Jouan, S. Ferre, M. Carras, M. Brun, D. Mechin, J.-L. Adam, and J. Troles, "Highly birefringent chalcogenide optical fiber for polarization-maintaining in the 3–8.5 μm mid-IR window," *Opt. Express* **24**(8), 7977–7986 (2016).

28. P. Cheben, J. H. Schmid, S. Wang, D.-X. Xu, M. Vachon, S. Janz, J. Lapointe, Y. Painchaud, and M.-J. Picard, "Broadband polarization independent nanophotonic coupler for silicon waveguides with ultra-high efficiency," *Opt. Express* **23**(17), 22553–22563 (2015).
29. M. Papes, P. Cheben, W. N. Ye, J. H. Schmid, D.-X. Xu, S. Janz, D. Benedikovic, C. A. Ramos, R. Halir, A. Ortega-Moñux, A. Delage, and V. Vašinek, "Fiber-chip edge coupler with large mode size for silicon photonic wire waveguides," *Opt. Express* **24**(5), 5026–5038 (2016).
30. D. Taillaert, P. Bienstman, and R. Baets, "Compact efficient broadband grating coupler for silicon-on-insulator waveguides," *Opt. Lett.* **29**(23), 2749–2751 (2004).
31. T. Tamir and S. T. Peng, "Analysis and design of grating couplers," *Appl. Phys. (Berl.)* **14**(3), 235–254 (1977).
32. L. Chrostowski and M. Hochberg, *Silicon Photonics Design: From Devices to Systems* (Cambridge University Press, 2015).
33. Z. Xiao, T.-Y. Liow, J. Zhang, P. Shum, and F. Luan, "Bandwidth analysis of waveguide grating coupler," *Opt. Express* **21**(5), 5688–5700 (2013).
34. M. Passoni, D. Gerace, L. Carroll, and L. C. Andreani, "Grating couplers in silicon-on-insulator: The role of photonic guided resonances on lineshape and bandwidth," *Appl. Phys. Lett.* **110**(4), 041107 (2017).
35. Y. Wang, W. Shi, X. Wang, Z. Lu, M. Caverley, R. Bojko, L. Chrostowski, and N. A. F. Jaeger, "Design of broadband subwavelength grating couplers with low back reflection," *Opt. Lett.* **40**(20), 4647–4650 (2015).
36. J. D. Joannopoulos, S. Johnson, J. N. Winn, and R. D. Meade, *Photonic Crystals: Molding the Flow of Light* (Princeton University Press, 2011).
37. C. Alonso-Ramos, A. Ortega-Moñux, I. Molina-Fernández, P. Cheben, L. Zavargo-Peche, and R. Halir, "Efficient fiber-to-chip grating coupler for micrometric SOI rib waveguides," *Opt. Express* **18**(14), 15189–15200 (2010).
38. C. Alonso-Ramos, A. Ortega-Moñux, L. Zavargo-Peche, R. Halir, J. de Oliva-Rubio, I. Molina-Fernández, P. Cheben, D.-X. Xu, S. Janz, N. Kim, and B. Lamontagne, "Single-etch grating coupler for micrometric silicon rib waveguides," *Opt. Lett.* **36**(14), 2647–2649 (2011).
39. M. Fischer, T. Galstian, R. Vallée, and A. Salimnia, "Surface and volume contributions to total diffractive efficiency in As_2S_3 thin film glasses," *Synth. Met.* **127**(1-3), 303–306 (2002).
40. D. Marcuse, "Loss Analysis of Single-Mode Fiber Splices," *Bell Syst. Tech. J.* **56**(5), 703–718 (1977).
41. "Corning(R) SMF-28(R) Ultra Optical Fiber," <https://www.corning.com/media/worldwide/coc/documents/Fiber/SMF-28Ultra.pdf>.
42. S. J. Orfanidis, *Electromagnetic Waves and Antennas* (2002).
43. L. Zavargo-Peche, A. Ortega-Moñux, J. G. Wangüemert-Pérez, and Í. Molina-Fernández, "Fourier based combined techniques to design novel sub-wavelength optical integrated devices," *Prog. Electromagnetics Res.* **123**, 447–465 (2012).
44. P. Cheben, R. Halir, J. H. Schmid, H. A. Atwater, and D. R. Smith, "Subwavelength integrated photonics," *Nature* **560**(7720), 565–572 (2018).
45. R. Halir, A. Ortega-Moñux, D. Benedikovic, G. Z. Mashanovich, J. G. Wangüemert-Perez, J. H. Schmid, I. Molina-Fernandez, and P. Cheben, "Subwavelength-Grating Metamaterial Structures for Silicon Photonic Devices," *Proc. IEEE* **106**(12), 2144–2157 (2018).
46. F. Fesharaki, N. Hossain, S. Vigne, M. Chaker, and K. Wu, "Accurate theoretical and experimental characterization of optical grating coupler," *Opt. Express* **24**(18), 21027–21037 (2016).
47. D. Taillaert, W. Bogaerts, P. Bienstman, T. F. Krauss, P. Van Daele, I. Moerman, S. Versteuyft, K. De Mesel, and R. Baets, "An out-of-plane grating coupler for efficient butt-coupling between compact planar waveguides and single-mode fibers," *IEEE J. Quantum Electron.* **38**(7), 949–955 (2002).
48. D. Taillaert, F. Van Laere, M. Ayre, W. Bogaerts, D. Van Thourhout, P. Bienstman, and R. Baets, "Grating couplers for coupling between optical fibers and nanophotonic waveguides," *Jpn. J. Appl. Phys.* **45**(8A), 6071–6077 (2006).